SCIENTIFIC REPORTS
nature research

OPEN

Characterization of the nucleotide-binding domain NsrF from the BceAB-type ABC-transporter NsrFP from the human pathogen *Streptococcus agalactiae*

Fabia Furtmann[1,5], Nicola Porta[2,5], Dai Tri Hoang[1], Jens Reiners[3], Julia Schumacher[1], Julia Gottstein[1], Holger Gohlke[2,4] & Sander H. J. Smits[1,3]✉

Treatment of bacterial infections is a great challenge of our era due to the various resistance mechanisms against antibiotics. Antimicrobial peptides are considered to be potential novel compound as antibiotic treatment. However, some bacteria, especially many human pathogens, are inherently resistant to these compounds, due to the expression of BceAB-type ABC transporters. This rather new transporter family is not very well studied. Here, we report the first full characterization of the nucleotide binding domain of a BceAB type transporter from *Streptococcus agalactiae*, namely *Sa*NsrF of the transporter *Sa*NsrFP, which confers resistance against nisin and gallidermin. We determined the NTP hydrolysis kinetics and used molecular modeling and simulations in combination with small angle X-ray scattering to obtain structural models of the *Sa*NsrF monomer and dimer. The fact that the *Sa*NsrF$_{H202A}$ variant displayed no ATPase activity was rationalized in terms of changes of the structural dynamics of the dimeric interface. Kinetic data show a clear preference for ATP as a substrate, and the prediction of binding modes allowed us to explain this selectivity over other NTPs.

Therapeutic compounds against bacterial infections are currently one of the biggest needs worldwide. Among antibiotics, antimicrobial peptides (AMP) offer promising potential for the treatment of bacterial infections, alone or in combination with already known molecules[1,2]. An alarming number of pathogenic multidrug resistant strains have evolved under the selective pressure caused by decades of incorrect antibiotic usage. Among them, methicillin-resistant *Staphylococcus aureus* (MRSA) or vancomycin-resistant *Enterococcus* (VRE) pose a high risk to therapeutic regimens[3]. To include new classes of antibiotics in therapy, studies were performed with lantibiotics, a class of AMPs. These ribosomally-synthesized peptides exhibit high potency against several human pathogenic bacterial strains[2–4] and show high stability to chemical and enzymatic degradation due to multiple intramolecular thioether rings and unsaturated amino acids[4–8].

Most known lantibiotics act similar in that they inhibit cell wall synthesis[9]. A common target for AMPs is the peptidoglycan layer, which exists in Gram-positive as well as Gram-negative bacteria. It is built up by altering amino sugars such as *N*-acetylglucosamine (GlcNAc) and *N*-acetylmuramic acid (MurNAc) and stabilized by a cross-linkage of those polymer chains. The inhibition of the cell wall synthesis results in reduced cell growth

[1]Institute of Biochemistry, Heinrich-Heine-Universität Düsseldorf, Universitätsstraße 1, 40225 Düsseldorf, Germany. [2]Institute for Pharmaceutical and Medicinal Chemistry, Heinrich-Heine-Universität Düsseldorf, Universitätsstraße 1, 40225 Düsseldorf, Germany. [3]Center for Structural Studies, Heinrich-Heine-Universität Düsseldorf, Universitätsstraße 1, 40225 Düsseldorf, Germany. [4]John von Neumann Institute for Computing (NIC), Jülich Supercomputing Centre (JSC), Institute of Biological Information Processing (IBI-7: Structural Biochemistry),, Forschungszentrum Jülich GmbH, Wilhelm-Johnen-Straße, 52425 Jülich, Germany. [5]These authors contributed equally: Fabia Furtmann and Nicola Porta. ✉email: sander.smits@hhu.de

and subsequent cell death. The well-known lantibiotic nisin contains five lanthionine rings and primarily targets the cell wall precursor Lipid II. The initial binding of the first two N-terminal lanthionine rings (A and B) of the lantibiotic to Lipid II is followed by a reorientation of the C-terminus into the membrane, resulting in pore formation and subsequently cell lysis[10,11]. Even though lantibiotics are effective in the nanomolar range, their application is hampered by resistance-conferring mechanisms found in human pathogenic bacteria[7,12,13]. The resistance is mediated by a newly discovered class of ATP binding cassette transporters, called Bacitracin efflux ABC transporters (BceAB), named after their first discovery in the bacitracin resistant strain of *Bacillus subtilis*[14,15]. In *Streptococcus agalactiae* such a BceAB-type ABC transporter is also present, as part of an operon that confers resistance against the lantibiotic nisin[16]. This operon consists of the membrane-associated protease *Sa*Nsr[17], the ABC transporter *Sa*NsrFP[8], and the two-component system comprising the response regulator *Sa*NsrR and the histidine kinase *Sa*NsrK[18]. So far, structural information is known only for *Sa*Nsr[17] and *Sa*NsrR[18].

Like all ABC transporters, BceAB-type transporters are composed of a nucleotide-binding domain (NBD) and a transmembrane domain (TMD). The NBD hydrolyses ATP, which drives conformational changes in the TMD, leading to substrate translocation. The TMD of BceAB-type ABC transporters are characterized by ten predicted transmembrane helices and a large extracellular domain (ECD_L) of ~ 220 amino acids that is the hallmark of this transporter family[4,8,16].

Sequences of the TMD domains from various BceAB-type ABC transporters are not very similar, which explains the large variety of substances they are able to translocate[16]. In contrast, NBDs share sequence and distinct motifs which are highly conserved throughout the ABC transporter superfamily[19–22]. NBDs are mainly L-shaped and comprise a helical signaling domain and a catalytic domain built of α-helices and β-strands[23–25]. The catalytic domain contains the Walker A motif that forms the nucleotide-binding site. A glutamate residue in the Walker B motif takes part in proper nucleotide binding; the γ-phosphate of the ATP molecule is sensed by a conserved histidine (H-loop) which when mutated results in an inactive variant[22,23,26]. Signaling and catalytic domains are connected by the Q- and the P-loop. Within the signaling domain the C-loop is located, which is the signature motif of an ABC transporter (for an alignment see Fig. S6 and Table S2)[22,27,28].

Dimerization of two NBD monomers in a head-to-tail conformation, is needed to enable ATP hydrolysis with the nucleotide binding sites located in the dimer interface. Each ATP molecule is sandwiched between the Walker A motif of one monomer and the C-loop of the second one, which results in a closed, stable complex[24,29–31]. An interaction between the NBD and the nucleotide is supposed to occur by π–π-stacking between the aromatic ring system of the nucleotide and an aromatic residue of the protein (F or Y). Hence, no preference towards any nucleotide-triphosphate (NTP) has been assumed[24], as also observed for example for yeast PDR5[32]. The hydrolysis of ATP is coupled to the presence of a cofactor, almost exclusively Mg^{2+}, which is coordinated by the Walker B motif. The divalent cation participates in the hydrolytic attack on the γ-phosphate of the nucleotide[26,28,31].

Here, we report for the first time biochemical and structural characteristics of the BceA nucleotide binding domain *Sa*NsrF, through NTP hydrolysis assays, molecular modeling and simulations. *Sa*NsrF is part of the BceAB-type ABC transporter NsrFP from *Streptococcus agalactiae*[16]. We show that the NBD $SaNsrF_{WT}$ and its hydrolysis-deficient variant $SaNsrF_{H202A}$ are monomeric in solution. Broad-ranging in vitro ATPase screenings delivered detailed information about the protein's properties with regard to its structure and physiology. We show that the preferred substrate of *Sa*NsrF is ATP as demonstrated by its kinetic parameters. Moreover, we built a structural model of the ATP/Mg^{2+}-bound *Sa*NsrF protein in its monomeric and dimeric form by comparative modeling and molecular dynamics simulations. In all, this constitutes the first biochemical characterization of a BceAB-type NBD.

Results

Cloning, expression and purification. For substrate transport BceAB-type ABC transporters depend on energy supply generated by ATP hydrolysis, which is mediated by the NBD. Here, we characterized the NBD NsrF of the BceAB-type ABC transporter NsrFP from *Streptococcus agalactiae*. To heterologously express $SaNsrF_{WT}$ and $SaNsrF_{H202A}$, we constructed expression vectors using a codon-optimized version of *Sa*NsrF for the heterologous expression in *E. coli* (Gen Bank accession number: WP_000923537). These constructs expressed a *Sa*NsrF protein with an N-terminal His10-tag attached for purification using Metal Ion Affinity Chromatography. The corresponding *Sa*NsrF constructs were expressed under the control of the plasmid-based T7-promoter via induction with Isopropyl-β-D-thiogalactopyranoside (IPTG). $SaNsrF_{WT}$ was purified to high homogeneity (Fig. 1A), and was examined by Size Exclusion Chromatography coupled to Multiangle Light Scattering (SEC-MALS)[33], which revealed a molecular mass of 31.9 ± 0.4 kDa for the $SaNsrF_{WT}$ protein (Fig. 1B). This corresponds nicely with the calculated theoretical molecular mass of the recombinant monomer of 30.9 kDa including the His10-tag. Thus, the conducted SEC-MALS analysis revealed that $SaNsrF_{WT}$ exists as a stable monomer in solution, which is in line with previous observations of other NBDs from different ABC transporter families[34–36].

By sequence alignments, His_{202} was identified to be the essential residue of the H-loop[37–39]. As shown for other NBDs, a point mutation to alanine results in a loss of the ATPase activity of the NBD. We generated this variant of *Sa*NsrF ($SaNsrF_{H202A}$), which indeed displayed no NTP hydrolysis (see below). This variant served as a negative control in all our experiments. The lack of NTP hydrolysis for $SaNsrF_{H202A}$ is in line with in vivo studies that show that this variant abolishes the activity of *Sa*NsrFP[8,40].

Activity of $SaNsrF_{WT}$. After successful purification, we functionally characterized $SaNsrF_{WT}$. To do so, we screened the following parameters for their influence on the ATP hydrolysis velocity: (I) pH, (II) salt concentration, (III) nature of the divalent ion and (IV) temperature (see Supporting Information and Fig. S1). As a result, the optimized conditions were found to be 100 mM HEPES at pH 7 with 0 mM NaCl as an assay buffer. The

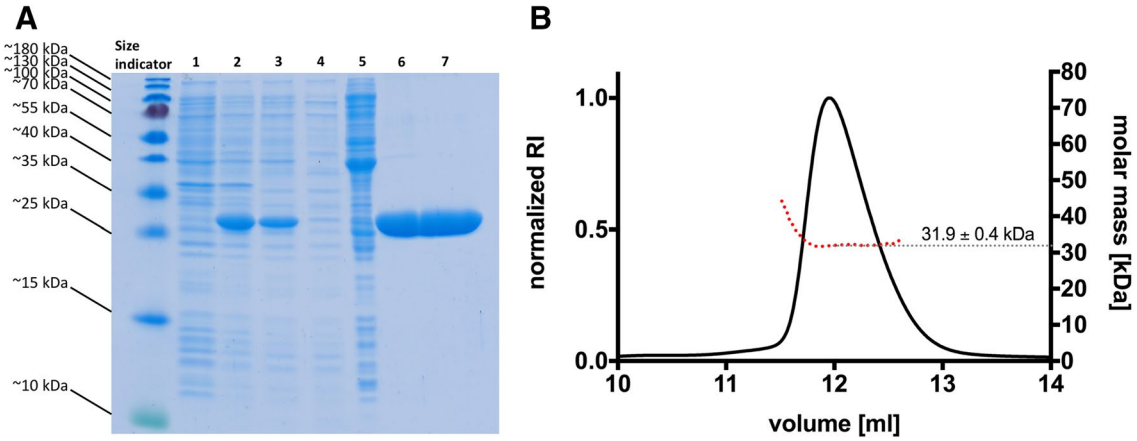

Figure 1. Purification and SEC-MALS of *Sa*NsrF$_{WT}$. (**A**) SDS-PAGE of the *Sa*NsrF$_{WT}$ purification progress. PageRuler Prestained Protein Ladder (size indicator; 10 to 180 kDa), *E. coli* strain before IPTG induction (1), *E. coli* strain after IPTG induction (2), IMAC load (3), IMAC flow-through (4), IMAC wash-fraction (5), IMAC eluate (6), SEC eluate (7). (**B**) Multiangle Light Scattering of *Sa*NsrF$_{WT}$. Freshly purified *Sa*NsrF$_{WT}$ was diluted in MALS-buffer and applied with a concentration of 3 mg mL^{-1} onto a Superdex 75 16/300 increase column. MALS-RI analysis shows that the *Sa*NsrF$_{WT}$ protein elutes with an absolute molecular mass of 31.9 ± 0.4 kDa, consistent with a theoretical monomeric mass in solution.

buffer included 10 mM Mg^{2+} and the reaction was finally performed at 30 °C, with an incubation time of 18 min (Fig S1). These optimized conditions were applied in all following experiments.

Velocity of NTP hydrolysis by SaNsrF$_{WT}$ and SaNsrF$_{H202A}$. Kinetic measurements were performed by quantifying the NTP hydrolysis under increasing concentrations of the respective nucleotide. We determined the NTP hydrolysis behaviour of *Sa*NsrF$_{WT}$ and *Sa*NsrF$_{H202A}$ using increasing amounts of ATP, GTP, CTP or UTP.

As depicted in Fig. 2A, the *Sa*NsrF$_{WT}$ protein demonstrated a nonlinear dependency of ATPase activity over a range of 0–5 mM ATP. The maximal reaction velocity was calculated to be 190.9 ± 10.0 nmol min^{-1} mg^{-1} when using ATP. Moreover, the calculation of the kinetic parameters resulted in a kinetic constant of k_{half} = 0.41 ± 0.05 mM and a Hill coefficient of h = 1.72 ± 0.27 (Fig. 2A and Table 1). A Hill coefficient > 1 demonstrates a cooperative behaviour, and suggests that *Sa*NsrF$_{WT}$ needs to dimerize to hydrolyze ATP, which is in line with other previously characterized NBDs[41–43]. For GTP, the maximal reaction velocity was 221.6 ± 11.1 nmol min^{-1} mg^{-1} with a Hill coefficient of h = 1.82 ± 0.27 and a k_{half} value of 0.69 ± 0.07 mM (Fig. 2B and Table 1). Interestingly, the highest reaction velocity with a value of 339.0 ± 30.4 nmol min^{-1} mg^{-1} was reached using CTP as a substrate with the highest measured k_{half} value of 1.23 ± 0.20 mM and a Hill coefficient of 1.63 ± 0.53 (Fig. 2C and Table 1). The kinetic parameters using UTP as a substrate resulted in comparably high values of v_{max} = 314.8 ± 23.4 nmol min^{-1} mg^{-1}, k_{half} = 0.90 ± 0.13 mM and h = 1.55 ± 0.25 (Fig. 2D and Table 1). The variant *Sa*NsrF$_{H202A}$ displayed no hydrolytic activity for any of the four used NTPs (Fig. 2, dashed lines).

Structural models of SaNsrF monomer and dimer. Since no experimental structure of *Sa*NsrF is available, we generated a structural model of the NBD by comparative modeling. NBDs are the most conserved parts of ABC transporters and in the case of *Sa*NsrF, the templates used for modeling show a sequence identity of ~ 30–40% and a sequence similarity of 84–89% (Table S1). Of these X-ray structures (resolution between 1.7 and 3.4 Å), two constitute NBDs in the functionally active assembly; they were crystallized with the TMD of the macrolide exporter MacAB from *Acinetobacter baumannii* (PDB ID 5GKO[44]) and MacAB-like from *Streptococcus pneumoniae* (PDB ID 5XU1[45]).

The homology model of *Sa*NsrF$_{WT}$ in the monomeric form is of high quality, given the low overall TopScore[46] (TS) value of 0.24 (Fig. 3A). This superimposition-free score evaluates local distance differences[47] of all atoms in a model, and a value closer to zero indicates higher quality. The regions modeled with lower reliability (TS > 0.5), accounting only for ~ 6% of the total sequence, are located at the β-hairpin (residues 15–18) and the two C-terminal helices (residues 229–232, 235–236, 246–250). Both substructures can be found in other NDBs, however, indicating the plausibility of the model. For example, when compared to the structure of ComA from *Streptococcus mutans* (PDB ID 3VX4[48]), the C-terminal helices have a virtually identical fold, with an RMSD of 0.6 Å for the last 50 residues, based on sequence alignment followed by structural superimposition.

The dimeric *Sa*NsrF$_{WT}$ model is structurally similar to other known structures, given RMSD values of ~ 5 Å or lower (RMSD of 3.5 Å, 4.5 Å and 5.2 Å for PDB IDs 1L2T, 5GKO, and 5XU1, respectively), indicating the suitability of the performed protein–protein docking. The reliability of the model is additionally verified by the presence of conserved motifs (Fig. 2B and Table S2), such as the phosphate-binding loop (P-loop or Walker A motif), the cofactor-chelating region (Walker B motif), and a short consensus sequence "LSGGQ" (C-loop or ABC signature motif), which signify ABC transporter family membership at the sequence level. Moreover, the α-helical and RecA-like domains are in the canonical head-to-tail arrangement (Fig. 3C). Interestingly, the

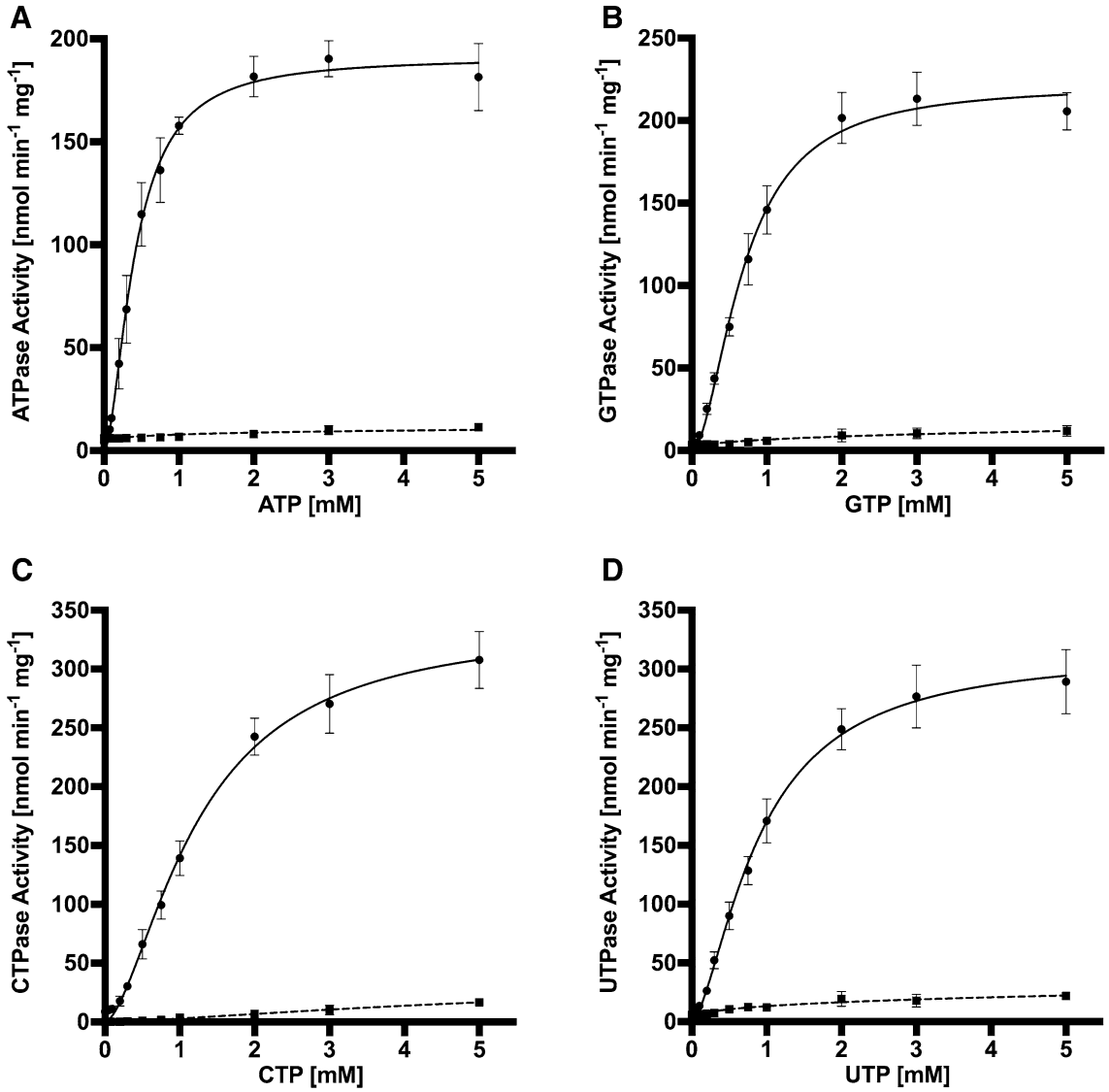

Figure 2. Kinetic measurement of *Sa*NsrF$_{WT}$ (black) and *Sa*NsrF$_{H202A}$ (dashed lines) NTPase Activity [nmol min^{-1} mg^{-1}] after 18 min of incubation. A concentration range of each NTP from 0 to 5 mM was applied on freshly purified *Sa*NsrF or *Sa*NsrF$_{H202A}$ (0.1 mg mL^{-1}; diluted in 100 mM HEPES at pH 7). The reaction was stopped after 18 min and dyed for 7 min. A sigmoidal fit was applied using GraphPad PRISM 8.3.0. (**A**) Kinetic parameters of *Sa*NsrF$_{WT}$ exposed to 0–5 mM ATP: v_{max}: 190.9 ± 10.0 [nmol min^{-1} mg^{-1}], h: 1.72 ± 0.27, k_{half}: 0.41 ± 0.05 [mM]. (**B**) Kinetic parameters of *Sa*NsrF$_{WT}$ exposed to 0–5 mM GTP: v_{max}: 221.6 ± 11.1 [nmol min^{-1} mg^{-1}], h: 1.82 ± 0.27, k_{half}: 0.69 ± 0.07 [mM]. (**C**) Kinetic parameters of *Sa*NsrF$_{WT}$ exposed to 0–5 mM CTP: v_{max}: 339.0 ± 30.4 [nmol min^{-1} mg^{-1}], h: 1.63 ± 0.53, k_{half}: 1.23 ± 0.20 [mM]. (**D**) Kinetic parameters of *Sa*NsrF exposed to 0–5 mM UTP: v_{max}: 314.8 ± 23.4 [nmol min^{-1} mg^{-1}], h: 1.55 ± 0.25, k_{half}: 0.90 ± 0.13 [mM]. All experiments have been performed in at least three biological replicates and are represented as means ± s.d.

NTP	V_{max}	k_{half}	h
ATP	190.9 ± 10.0	0.41 ± 0.05	1.72 ± 0.27
GTP	221.6 ± 11.1	0.69 ± 0.07	1.82 ± 0.27
CTP	339.0 ± 30.4	1.23 ± 0.20	1.63 ± 0.53
UTP	314.8 ± 23.4	0.90 ± 0.13	1.55 ± 0.25

Table 1. Kinetic parameters V_{max} [nmol min^{-1} mg^{-1}], k_{half} [mM] and the Hill-coefficient h resulting from different NTPs as a substrate for *Sa*NsrF$_{WT}$. All experiments have been performed in at least three biological replicates and are represented as means ± s.d.

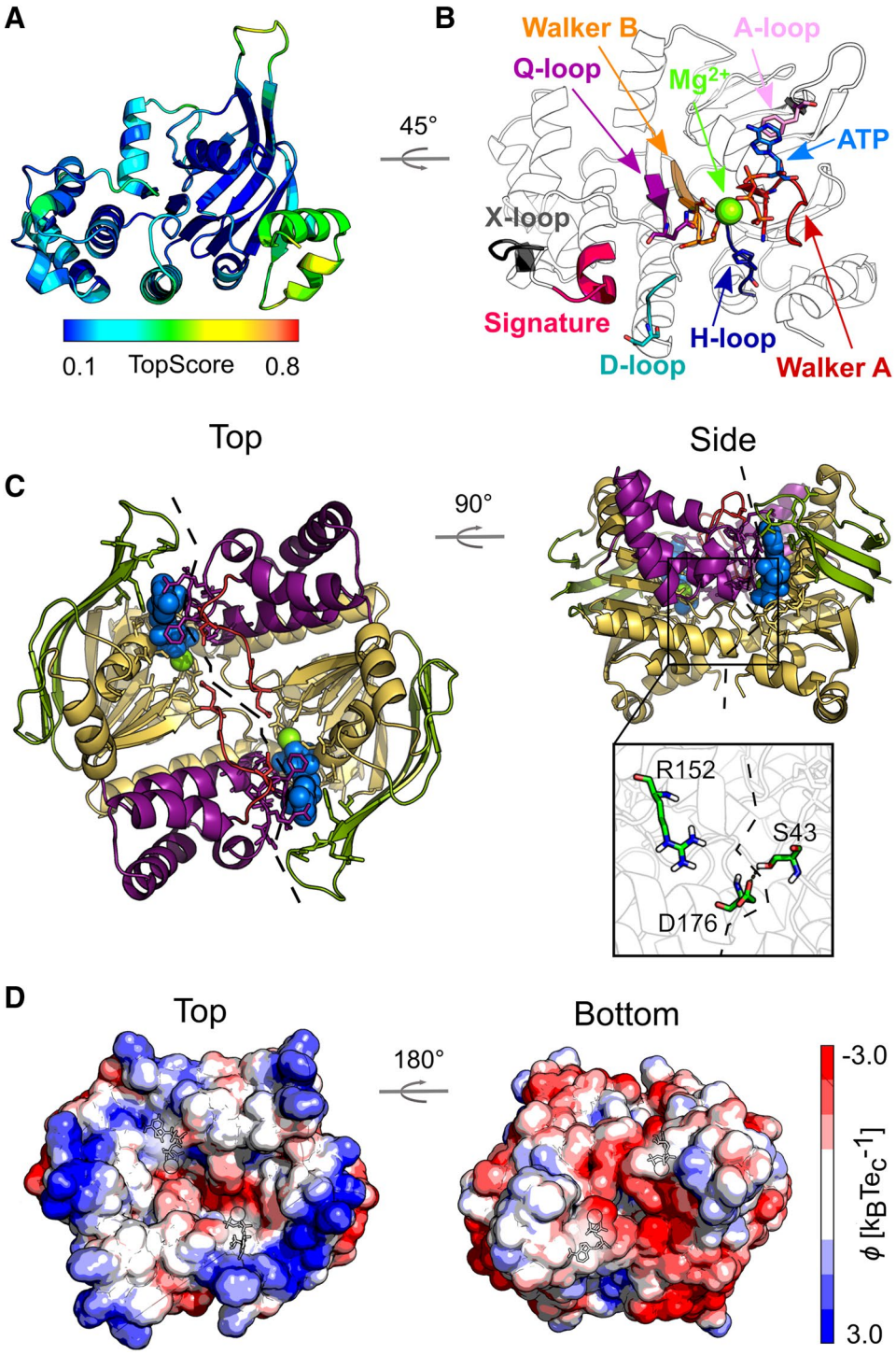

Figure 3. Homology models of *Sa*NsrF$_{WT}$ monomer (**A**, **B**) and dimer (**C**, **D**). (**A**) Structure colored according to the residue-wise TopScore. Green/yellow colors indicate regions with low residue-wise error (< 50%). (**B**) Zoom into the NBD-NBD interface with ATP and Mg^{2+} bound, highlighting the conserved motifs necessary for ATP binding and hydrolysis, and for NBD-NBD and NBD-TM communication. See Table S2 for the location of the conserved motifs in the primary sequence[22]. (**C**) Structure colored according to domain organization and zoom into the NBD–NBD interface, reporting the conserved residues used as restraints for protein–protein docking. The α-helical domain is shown in violet; the RecA-like domain, further subdivided into F1-type ATP binding core, antiparallel β subdomain, and γ-phosphate linker is colored respectively in yellow, green, and red. The bound ATP (blue) and Mg^{2+} (green) are shown in space-filling representation. The dashed line highlights the interface between subunits. (**D**) Electrostatic potential computed for the representative structure of the most populated cluster of conformations obtained by MD simulations. The color scale of the electrostatic potential ranges from − 3.0 (red) to + 3.0 (blue) $k_BTe_c^{-1}$; the potentials were computed with the Adaptive Poisson-Boltzmann Solver (APBS)[49].

calculated electrostatic potential shows a clear polarization (Fig. 3D) with positively charged residues (such as R and K) prevalent on the dimer's side oriented towards the membrane (named "top") and negatively charged residues (such as D and E) on the opposite side (named "bottom") in agreement with the expected topology.

Structural dynamics at the NBD–NBD interface and impact of the SaNsrF$_{H202A}$ substitution. The *Sa*NsrF models were subjected to all-atom MD simulations of in total 10 µs length to investigate the structural dynamics at the NDB-NDB interface and to highlight the impact of the H202A substitution on ATP/Mg^{2+} binding. The RMSD profiles for *Sa*NsrF$_{WT}$ and *Sa*NsrF$_{H202A}$ monomers (Fig. S2) reach almost immediately a plateau at ~ 4 Å, indicating that the overall structure is mostly invariant over simulation times of 0.5 µs for each replica. Additionally, the low variability of ATP/Mg^{2+} coordinates (Fig. S3A,B) suggests that the *Sa*NsrF$_{H202A}$ substitution does not impact ATP/Mg^{2+} binding, at least on the timescale of our simulations.

The RMSD profile for the *Sa*NsrF$_{WT}$ and *Sa*NsrF$_{H202A}$ dimers is mostly invariant (Fig. S4A) when the structures are superimposed onto the two subunits separately (red and blue lines). However, when the superimposition is done with respect to the least mobile regions in the whole dimer (black line), RMSD values reach ~ 6–9 Å in three out of five replicas for *Sa*NsrF$_{WT}$, indicating that the arrangement of the two subunits changes during the simulations. In particular, the interface between the subunits partially opens (Fig. S4B) up to ~ 25 Å (Fig. S5). The change of ATP molecule and Mg^{2+} ion positions relative to the protein is more marked for *Sa*NsrF$_{WT}$ dimer (Fig. S3). Interestingly, this is not happening in the *Sa*NsrF$_{H202A}$ variant, where the interface seems to be more stable.

In terms of structural mobility, the central region of *Sa*NsrF$_{WT}$ and *Sa*NsrF$_{H202A}$ (residues ~ 50–150) shows a different profile in monomers and dimers (Fig. 4). In monomers (Fig. 4A,B), this region is less mobile than in dimers (Fig. 4C,D), with RMSF values lower than 2 Å and up to 4 Å, respectively. Moreover, in the dimeric *Sa*NsrF$_{H202A}$ variant, this region is slightly less mobile than in *Sa*NsrF$_{WT}$. The residues of the central region are oriented towards the TM region of the transporter (Fig. 4E,D). In addition, after the alignment of *Sa*NsrF with NBDs of structures containing the TMD (PDB ID 5XU1, Fig. 4G), most of the residues of this central region are located at < 5 Å distance from the coupling helices (CH1, between TM2 and TM3, and C-terminal CH2) of the transporter, suggesting that this central region is involved in NBD-TMD communication (Fig. 4H). A similar result was found for the HlyB transporter[50], where the X-loop motif (corresponding to residues 137–142 in *Sa*NsrF, located in the central region) has been proposed to be an important part of the NBD-TMD communication. Even though we are considering an ATP-bound pre-hydrolysis state, *Sa*NsrF in the dimer seems to be generally more mobile than in the monomer, in agreement with the idea that a dimeric assembly is needed in order to perform its function.

H-bond analysis in *Sa*NsrF$_{WT}$ and *Sa*NsrF$_{H202A}$ dimers reveals that the number of H-bond interactions between *Sa*NsrF and the ligands (ATP molecules and magnesium ions) is on average higher in the case of the *Sa*NsrF$_{H202A}$ variant (Fig. 5A). This is due to the higher structural stability compared to *Sa*NsrF$_{WT}$. Besides the three residues used as restraints for protein–protein docking (S43–R152–D176), other residues contribute to the stability of the dimer with H-bond occupancies up to 70%, such as R13, T14, R15, E42, E144, and R178 (Fig. 5B,C). Surprisingly, the residue-wise H-bond occupancy in *Sa*NsrF$_{WT}$ is significantly higher ($p < 0.01$) for two specific H-bonds involving both side chains and backbone atoms (D136–R15 and R133–R15), although the interface of the *Sa*NsrF$_{WT}$ dimer is less structurally stable (see above). Indeed, in the initial dimeric model, these interactions are not present, but require the movement of one monomer to the other for them to form.

To conclude, the generated models show a high structural stability over the simulation lengths. In the dimers, the central region is more mobile than in the monomers; in *Sa*NsrF$_{WT}$, the interface between subunits is structurally less stable than in the *Sa*NsrF$_{H202A}$ variant. Since a shift of one monomer to the other is necessary for NDBs to perform their function, these results together suggest that the mutation *Sa*NsrF$_{H202A}$ impacts the structural dynamics at the *Sa*NsrF interface and not only the catalytic mechanism.

Small angle X-ray scattering. Unfortunately, we were not able to crystalize the *Sa*NsrF protein, although extensively tried. In order to experimentally validate this new model, we choose Small Angle X-Ray Scattering (SAXS) to compare the theoretical model with the experimental scattering (Fig. 6A) measured with the Xenocs Xeuss 2. Based on the experimental data, we calculated an ab initio model for *Sa*NsrF$_{WT}$ with the program GASBOR[51] and obtained a χ^2 value of 0.97. Superimposing the ab initio and the TopModel model reveals that the structure and the envelope obtained by the SAXS experiment overlap, but also a density tail at the C-terminus of *Sa*NsrF$_{WT}$ (Fig. 6B) that is not occupied by the model. Scrutinizing the templates used by TopModel[52] shows that this helical part (Fig. 6B, orange helix) is rather unstructured or even missing. This finding indicated that this region might be highly flexible in solution, thereby covering the available free space in the SAXS envelope (Fig. 6B, red helix). With the program CRYSOL[53] we compared the theoretical scattering curve obtained from the TopModel model against the experimental data. The resulting χ^2 value of 1.16 indicates a good agreement between the prediction and the experiment. We uploaded the SAXS data and the corresponding model of *Sa*NsrF to the Small Angle Scattering Biological Data Bank (SASBDB)[54,55] with the accession code SASDJR3.

Molecular docking of other NTPs. In order to rationalize the hydrolysis preference for ATP over other NTPs, we predicted the binding mode of these molecules in complex with the *Sa*NsrF$_{WT}$ dimer. Ten different pocket conformations, obtained from five equilibrated structures used also for MD simulations times two pockets each, were considered. When focusing on the configurations with lowest Coulomb (ecoul) and van der Waals (evdw) energies, ATP is slightly enriched compared to the other NTP (3 × ATP, 2 × UTP, 1 × CTP and 1 × GTP), suggesting that ATP binding is preferred due to enthalpic contributions to binding (Fig. 7A). Residues giving rise to this preference are those interacting with the nucleobase, namely F12, T49, A23 of one subunit and F143′ and

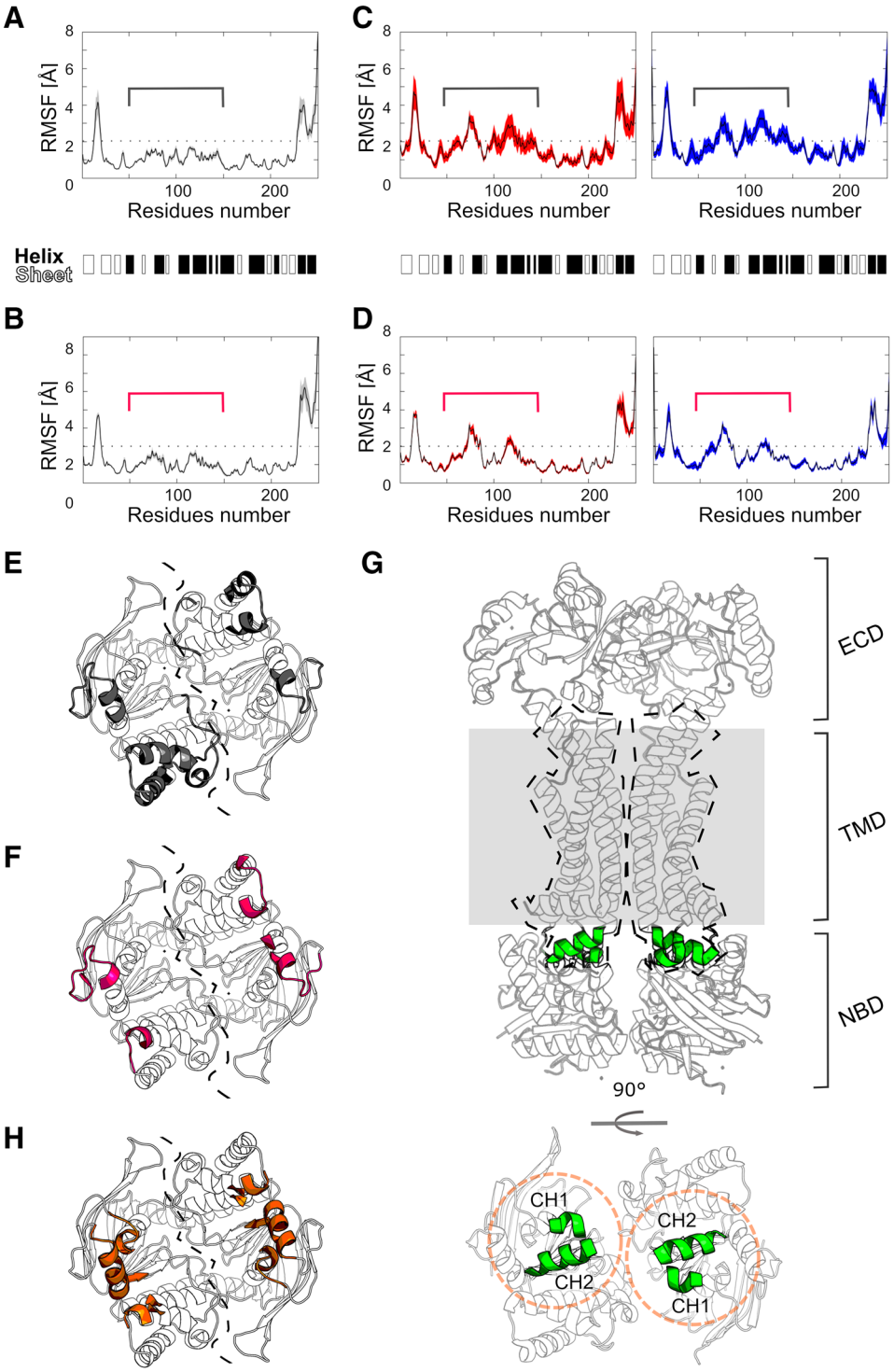

Figure 4. Structural mobility of the *Sa*NsrF$_{WT}$ and *Sa*NsrF$_{H202A}$ systems expressed as RMSF of Cα atoms. Before RMSF calculation, the structures were fitted onto the 15% least mobile residues, averaged over five MD simulation replicas. The variability between replicas is expressed as SEM and shown as colored area (grey for the monomers, red for chain A and blue for chain B). (**A**) *Sa*NsrF$_{WT}$ monomer. (**B**) *Sa*NsrF$_{H202}$ variant monomer. (**C**) *Sa*NsrF$_{WT}$ dimer. (**D**) *Sa*NsrF$_{H202}$ variant dimer. The secondary structure elements of the initial model are shown as black and white bands. The central region of *Sa*NsrF$_{H202}$ (residues ~ 50–150) is highlighted with brackets. Residues of the central region with RMSF > 2 Å are mapped onto the dimer structures. (**E**) For *Sa*NsrF$_{WT}$ (in grey) and (**F**) for *Sa*NsrF$_{H202}$ variant (in pink). The other two regions with RMSF > 2 Å (hairpin of the antiparallel β subdomain and the C-term) are not shown for clarity. The dashed line highlights the interface between subunits. (**G**) Structure of the MacAB-like transporter from *Streptococcus pneumoniae* (PDB ID 5XU1[45]) reported as comparison to highlight the expected orientation of the NBD to the TMD (shown as dashed shape), its coupling helices (CH1 and CH2, highlighted in green) and the membrane (as grey area). (**H**) After superimposition of the NBDs, regions of *Sa*NsrF located at < 5 Å from the coupling helices of the MacAB-like structure, and therefore likely involved in NBD-TMD communication, are highlighted in orange.

A

System	Replica	*Sa*NsrF$_A$-*Sa*NsrF$_B$	*Sa*NsrF-(ATP-Mg^{2+})
*Sa*NsrF$_{wt}$	I	6.29 (2.10)	15.54 (2.21)
	II	10.70 (3.12)	13.94 (2.05)
	III	8.07 (2.35)	15.19 (2.14)
	IV	9.02 (2.90)	13.24 (2.93)
	V	12.62 (3.20)	12.54 (2.05)
	All ± SEM	**9.34 ± 1.57**	**14.09 ± 1.15**
*Sa*NsrF$_{H202A}$	I	8.65 (2.39)	15.33 (2.05)
	II	9.51 (3.01)	14.64 (2.57)
	III	10.95 (2.85)	13.17 (2.41)
	IV	8.39 (2.34)	18.05 (2.39)
	V	18.05 (2.39)	18.66 (2.61)
	All ± SEM	**9.25 ± 1.30**	**15.97 ± 1.42**

**

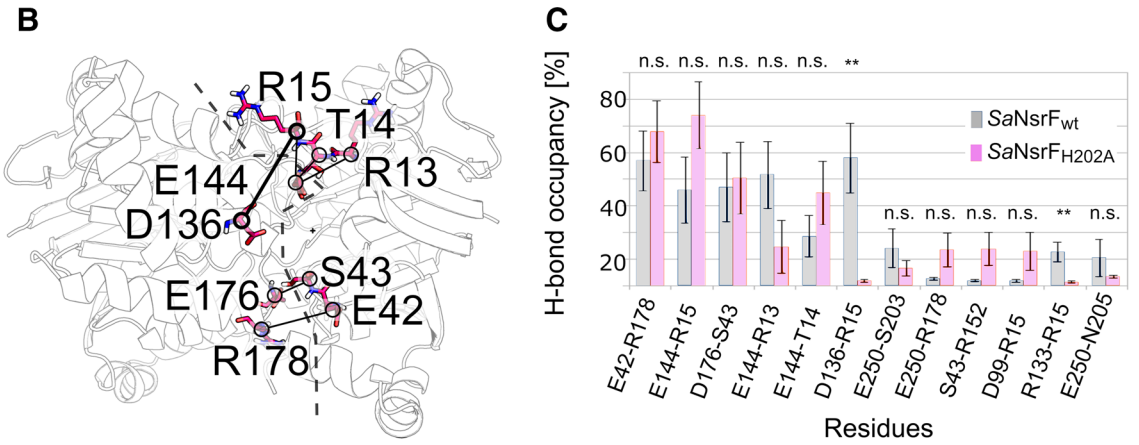

Figure 5. H-bond analysis in *Sa*NsrF$_{WT}$ and *Sa*NsrF$_{H202A}$ dimers. (**A**) The average number of H-bonds between the two proteins and between the protein and the ligands per MD replica. Standard deviations are reported in parentheses. For the numbers in bold, the SEM was computed according to $n = 5$. $^{**}p < 0.01$ according to a two-tailed *t*-test. (**B**) Residues in the interface that predominantly form H-bonds (occupancy > 20%). H-bonds are shown as lines connecting the Cα atoms of these residues. The dashed line highlights the interface between subunits. (**C**) H-bond occupancy for the most prevalent interactions (occupancy in at least one of the systems > 10%). Error bars are showing the SEM. $^{**}p < 0.01$ according to a two-tailed *t*-test for the comparison of *Sa*NsrF$_{WT}$ and *Sa*NsrF$_{H202A}$ variant; n.s.: not significant.

E144′ of the other (Fig. 7B). In particular, the phenylalanines are interacting with the nucleobase by π-π stacking interactions, and the amino groups of CTP and GTP form H-bonds with the backbone oxygen of F143′ and the carboxylate group of E144′, respectively. Since in ATP the amino group has the same orientation as in CTP, a similar kind of H-bond pattern can be expected.

Over respective pockets 1 or 2, which are not symmetric as described above, ATP shows the largest sums of Coulomb and van der Waals energies compared to the other NTPs (Fig. 7C), indicating strongest binding based on enthalpic components, which is in line with the biochemical data where ATP shows the lowest k_{half} value (Fig. 2 and Table 1).

Discussion

A rather novel family of ABC-transporters, the Bacitracin efflux (Bce) type transporters, have been identified to confer high-level resistance against bacitracin as well as against lantibiotics such as nisin and gallidermin in *Bacillus subtilis, Staphylococcus aureus,* and *Streptococcus agalactiae*[8,14,16,57–60]. These transporters have been rudimentarily characterized in vitro. We set out to characterize the NBD of the transporter *Sa*NsrFP; this transporter has been shown to be involved in lantibiotic resistance[8].

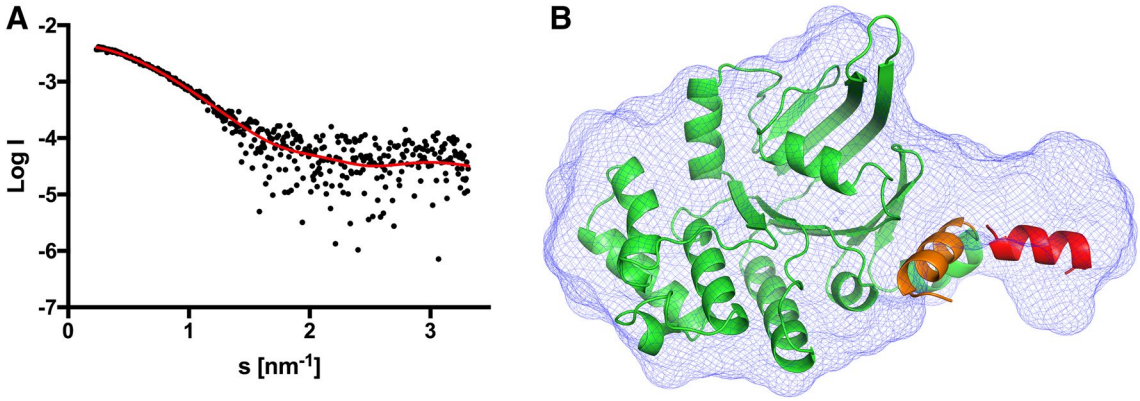

Figure 6. Comparison of the ab initio model with the homology model. (**A**) Experimental scattering data are shown as black dots and the ab initio model fit as red line. The intensity is displayed as a function of momentum transfer *s*. (**B**) Ab initio model of the *Sa*NsrF$_{WT}$. The volumetric envelope from *Sa*NsrF$_{WT}$, calculated from the scattering data using GASBOR[51], is shown by the blue mesh. The homology model of the *Sa*NsrF$_{WT}$ monomer (shown in green) was docked into the volumetric envelope using SUPCOMB[56]. Concerning the flexibility of the C-terminal helix (shown in orange), we show a possible, changed orientation of this helix in red.

We have purified and characterized the *Sa*NsrF$_{WT}$ and *Sa*NsrF$_{H202A}$ proteins regarding their ability of ATP hydrolysis. The results revealed that inorganic phosphate is only released in a pH range of 6–8, where an HEPES buffer at pH 7 was found to yield maximal ATPase activity. Interestingly, 20% difference could be found in a TRIS buffer system at the same pH (Fig S1A). Similar results were obtained by Zaitseva et al. examining the HlyB-NBD[36]. In that study, a correlation between the pH of 6 and the pK$_a$ values of the glutamate residue and/or the γ-phosphate of the nucleotide and between the pH of 8 and the pK$_a$ value of the conserved histidine bound in a salt bridge with the γ-phosphate was made. On that basis, the nucleophilic attack on the γ-phosphate is preceded, originating from a hydrolytic water molecule, which results in the cleavage of the γ-phosphate moiety[26,36,61]. Moreover, the importance of the conserved histidine could be confirmed since the *Sa*NsrF$_{H202A}$ variant was shown to be incapable of hydrolysing ATP. Here, the 'linchpin'-role during ATP-hydrolysis is conducted by the H-loop[22,36,38,62]. Also, this allows a possible explanation for the observed decrease of activity with increasing concentrations of NaCl (Fig. S1B). Since the conserved histidine is in contact with the γ-phosphate of the nucleotide by forming a salt bridge, rising salt concentration could disrupt this existing interaction. In contrast, a buffer system containing 300 mM of NaCl was used for protein storage, which indicates an inverse correlation between protein stability and activity at rising NaCl concentrations[63]. The incapability of *Sa*NsrF$_{H202A}$ to hydrolyse ATP supports in vivo studies where a loss of resistance against the lantibiotic nisin was observed when expressed in *L. lactis* bacterial cells[8].

Like many other NBDs, *Sa*NsrF was observed to be strictly dependent on its cofactor Mg^{2+}[39,64,65], because this is required as a Lewis acid in the catalytic cycle. Mg^{2+} is involved in proton abstraction from the nucleotide and the nucleophilic attack of the catalytic water, which results in the hydrolytic cleavage of its γ-phosphate[36].

Finally, we conducted kinetic measurements including all optimized parameters and the preference of *Sa*NsrF$_{WT}$ and *Sa*NsrF$_{H202A}$ for hydrolysing different NTPs. We propose that the main interaction of the nucleoside triphosphate and the protein occurs by π–π-stacking between the adenine moiety and F12 downstream of the Walker A motif (Fig. 3B,C) as also observed for other NBD's[22,24,25,30]. Also, Mg^{2+}, anchored to the protein through Asp and Glu residues of the Walker B motif, interacts with the phosphate region of ATP. The Walker A motif binds to the other side of the phosphate region (Fig. 3B).

Based on a comparison of docked binding poses of other NTPs, additional interacting residues were predicted (Fig. 7B). Amino group-containing NTPs (ATP, CTP and GTP) can form H-bonds with the backbone oxygen of F143′ and the carboxylate group of E144′, whereas purines in ATP and GTP form more extended π–π stacking interactions with F12 and F143′. ATP shows the largest sums of Coulomb and van der Waals energies compared to the other NTPs in either pocket of the NBD, in line with the biochemical data where ATP displayed the lowest k_{half} value (Fig. 2 and Table 1).

By comparing the measured kinetic parameters of each examined NTP, it becomes obvious that the reactions including UTP or CTP resulted in a significantly higher reaction velocity, respectively, when compared to ATP. Nevertheless, the CTPase and UTPase activities revealed noticeably high kinetic constants (k_{half}) as well. With regards to the substrate affinity represented by the k_{half} value, a minimum of 0.41 ± 0.05 mM was reached using ATP as a substrate, which signifies ATP as the most favoured of all four tested NTPs for *Sa*NsrF$_{WT}$. Hence, ATP has the highest affinity to *Sa*NsrF$_{WT}$ compared to the other examined NTPs, which corresponds with the physiological appearance in vivo of each NTP ([ATP] > [GTP] > [UTP] > [CTP]), which underlines that ATP is the preferred substrate for the protein[32,66–68]. Considering the physiology of purine (ATP, GTP) and pyrimidine (UTP, CTP) nucleotides, we concluded that the involved aromatic ring systems play a major role concerning the substrate affinity and stability of the protein-substrate-complex. Here, pyrimidine bases exhibit a smaller electron density that can be involved in π–π-stacking. Thus, dissociation of pyrimidine nucleotides from the enzyme occurs faster than purine nucleotides. By contrast, the stabilized protein–purine-complex is less liable

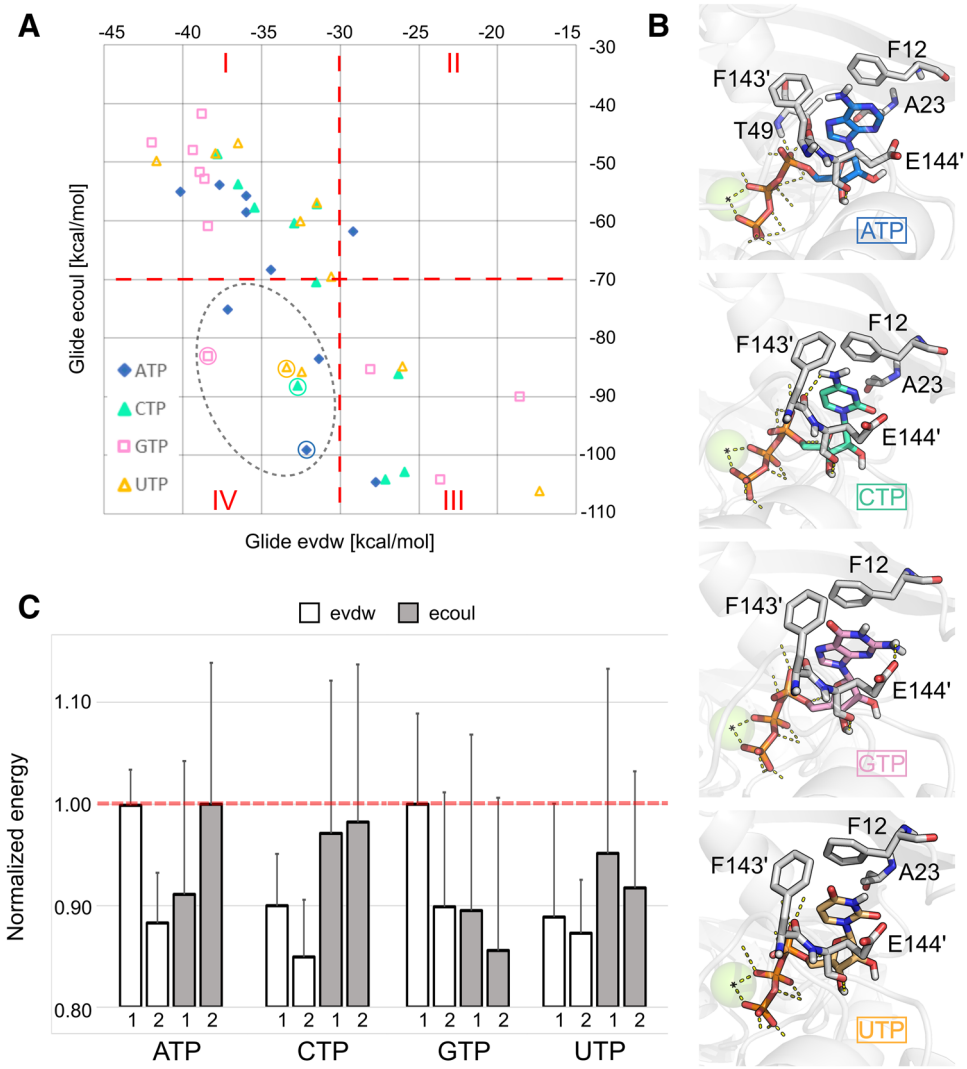

Figure 7. Molecular docking of other NTPs. (**A**) Scatterplot representing the Coulomb (ecoul) versus the van der Waals (evdw) energy terms of the docking score. Each data point represents an NTP configuration inside the two pockets of five different, equilibrated *Sa*NsrF structures. In quadrant IV, NTP configurations with respective lowest energies are circled. (**B**) Representative binding modes of NTPs, referring to the circled data points in section A. Residues at ≤ 4 Å from the nucleobases are shown in sticks and labelled. The Mg^{2+} ion is shown as a green sphere (**C**) Normalized average energy terms for pockets 1 and 2 of each SaNsrF complex. The error is reported as normalized SEM ($n = 5$).

to dissociation. Together, this may explain the small k_{half} values found for ATP and GTP and the high reaction velocities caused by a high turnover of CTP and UTP.

NBDs are assumed to share a large number of properties due to highly conserved sequences and specific motifs (see Fig. 3B,C and Table S2)[22–26,30]. The presence of a certain substrate such as ATP is supposed to induce a dimerization of the two NBD monomers in a typical head-to-tail formation, resulting in two ATP molecules in the dimer interface, sandwiched by the Walker A motif of one monomer and the signature motif of the other one as a cooperative process[22,24,25].

NBDs hydrolyse ATP, which drives substrate translocation by conformational changes of the TMD. In the case of the BceAB-type ABC transporter *Sa*NsrFP, the energy supply is provided by the BceA-domain *Sa*NsrF[16]. By employing SEC-MALS-coupled analysis we were able to confirm a monomeric state of $SaNsrF_{WT}$ and its variant $SaNsrF_{H202A}$ in solution since the measured molecular masses corresponded with the calculated values for each monomer. This agrees with the oligomeric state of other NBDs from other ABC transporter families in the absence of nucleotide[34–36].

Furthermore, this is in line with our SAXS data that allowed the construction of a volumetric envelope of the $SaNsrF_{WT}$ monomer. The experimental structure of *Sa*NsrF has not been published yet. Here, we generated a structural model using TopModel[52] based on five main templates 1F3O_A, 5XU1_B, 2PCL_A, 5GKO_A, 2OLJ_A (Fig. 3A, 6B). We compared this model with the volumetric envelope obtained from SAXS data, showing high

reliability and agreement with experimental data. It is striking that the density of the protein model is partly not occupied. A flexible C-terminus could be the reason, which would make a temporary fit of the versatile C-terminal helix to the proposed model possible. As for well-studied NBDs such as HisP, the modeled *Sa*NsrF dimer exhibits the typical head-to-tail formation including two sandwiched ATP molecules in the dimer interface between the Walker A motif of the first monomer and the C-loop of the second one[22,24,25,30]. Therefore, the *Sa*NsrF protein shares many structural similarities with other known NBDs. As the γ-phosphate moiety of ATP was predicted to be in close proximity of the conserved histidine (H-loop) and the cofactor Mg^{2+}, one can deduce a consensus with the hypothesis of the H-loop acting as a sensor, whereas the cofactor is involved in hydrolytic cleavage while being coordinated by the Walker B motif (Fig. 3B,C)[22,23,26,28]. Furthermore, in *Sa*NsrF$_{WT}$, the interface between subunits is structurally less stable than in *Sa*NsrF$_{H202A}$. Since a shift of one monomer to the other is necessary for NDBs to perform their function, these results suggest that the substitution *Sa*NsrF$_{H202A}$ impacts the structural dynamics at the *Sa*NsrF interface and not only the catalytic mechanism.

Clearly, the *Sa*NsrF protein represent an isolated NBD and we do not know if the kinetic correspond to the ATP hydrolysis that will occur in the presence of the transmembrane protein *Sa*NsrP. However, when comparing the data with known NBDs which has been described before in the presence and absence of the transmembrane segment it can be observed that v_{max} might be changed, the k_m values however remains very similar. For example the ATP hydrolysis kinetics have been described for the HlyB NBD as well as for the purified full length transporter in detergent solution[26,36,38,43,69]. Here the NBD showed a v_{max} of 200 nmol min^{-1} mg^{-1} with a k_m value of 0.31 where as the full length transporter displayed a lower v_{max} of 8.1 nmol min^{-1} mg^{-1} with a k_m value of 0.36. This reduction is likely due to the detergent, which is present to keep the HlyB transporter in solution. Important, however is that in both cases the kinetic displayed cooperativity (Hill coefficient > 1) as in the case of *Sa*NsrF and the corresponding histidine mutation also resulted in an inactive protein. This shows that our NTP analysis of the *Sa*NsrF will likely be similar even when the TMD *Sa*NsrP is present. The same observations were found for the nisin transporter NisT from *L. lactis*[70] and the nukacin ISK-1 transporter NukT from *Staphylococcus arneri* ISK-1[71] albeit in detergent solution.

In summary, the experiments revealed the first detailed insights into biochemical properties of the BceA domain of the BceAB-type ABC transporter *Sa*NsrFP. We showed that *Sa*NsrF$_{WT}$ and its variant *Sa*NsrF$_{H202A}$ exist as monomers in solution and determined several physiological and structural properties of the protein by evaluating its ATPase activity in comprehensive in vitro studies and molecular modelling and simulations. Hence, this study contributes to the mechanistic and structural understanding of the BceAB-type ABC transporter family, which opens up the possibility to pharmacologically target this family in order to combat multidrug-resistant species in the long run. It further confirms in vivo data where the H202A variant of *Sa*NsrF displayed a loss in the activity, which now can be pinpointed to a lack of ATP hydrolysis, and shows that this variant can well serve as a negative control in studies concerning BceAB type transporters since the histidine is conserved throughout the sequence of this family.

Materials and methods

Expression of SaNsrF$_{WT}$ and SaNsrF$_{H202A}$. *E. coli* BL21 (DE3) strains were transformed via heat shock method[72] with pET-16b-NHis$_{10}$-*Sa*NsrF$_{WT}$ or pET-16b-NHis$_{10}$-*Sa*NsrF$_{H202A}$, respectively. Precultures were selectively grown with 20 µg mL^{-1} ampicillin at 37 °C and 180 rpm overnight. Lysogeny Broth (LB) medium was pre-incubated with 20 µg mL^{-1} ampicillin and inoculated with the respective preculture to an OD_{600} of 0.1. The cultures were grown to an OD_{600} of 0.4 at 37 °C and 180 rpm whereupon the temperature was reduced to 18 °C. Protein expression was induced by the addition of 1 mM IPTG at an OD_{600} of 0.8 and the cultures were further grown overnight.

Protein purification. *Sa*NsrF$_{WT}$ and *Sa*NsrF$_{H202A}$ were purified using Immobilized Metal Ion Chromatography (IMAC). Therefore, a 5 mL HiTrap Chelating HP column, loaded with Zn^{2+}, was equilibrated with low IMAC-buffer (100 mM HEPES at pH 8, 300 mM NaCl, 20% glycerol). Protein elution was undertaken with the high IMAC-buffer (low IMAC-buffer plus 125 mM histidine). A washing step of 40-percent high IMAC-buffer was introduced before. The concentrated eluted proteins were then injected onto a Superdex 75 16/60 size exclusion column at a flow rate of 0.5 mL min^{-1}, pre-equilibrated with SEC buffer (100 mM HEPES at pH 8, 300 mM NaCl, 20% glycerol). Protein eluates were collected and stored at 4 °C.

ATPase activity assay. The ATPase activity of *Sa*NsrF$_{WT}$ and *Sa*NsrF$_{H202A}$ (diluted in 100 mM HEPES at pH 8, 100 mM NaCl) was examined by the Malachite Green Phosphate Assay at a protein concentration of 0.1 mg mL^{-1} that was initially undertaken at room temperature (20 °C). Several parameters were screened to determine the optimal buffer and temperature conditions for the protein activity (see Supplementary Information).

Kinetic measurements for *Sa*NsrF$_{WT}$ and *Sa*NsrF$_{H202A}$ were performed under the influence of NTP (ATP, GTP, CTP, UTP) with concentrations ranging from 0 to 5 mM.

Therefore, the kinetics were fitted using the Hill equation:

$$Y = \frac{v_{max} \times X^h}{\left(k_{half}^h + X^h\right)}.$$

Y: ATPase activity [nmol min^{-1} mg^{-1}], X: substrate concentration [mM], k_{half}: substrate concentration at half-maximal reaction velocity [mM], h: Hill coefficient.

All shown data are representing the average of a triple evaluation at least, with the standard deviation reported as errors.

Small angle X-ray scattering (SAXS). We collected all SAXS data on our Xeuss 2.0 Q-Xoom system from Xenocs, equipped with a PILATUS 3 R 300 K detector (Dectris) and a GENIX 3D CU Ultra Low Divergence x-ray beam delivery system (Xenocs). The chosen sample to detector distance for the experiment was 0.55 m, results in an achievable q-range of 0.18–6 nm^{-1}. All measurements were performed at 15 °C with protein concentrations between 0.5 and 4.2 mg mL^{-1}. Samples were injected in the Low Noise Flow Cell (Xenocs) via autosampler. For each sample, twelve frames with an exposer time of ten minutes were collected. By comparing these frames, we excluded the possibility of aggregation and radiation damage during the measurement. Data were scaled to absolute intensity against water. All used programs for data processing were part of the ATSAS Software package (Version 3.0.1), available on the EMBL website[73]. Primary data reduction was performed with the program PRIMUS[74]. With the Guinier approximation we determined the forward scattering $I(0)$ and the radius of gyration (Rg)[75]. The program GNOM was used to estimate the maximum particle dimension (D_{max}) with the pair distribution function $p(r)$[76]. Low resolution ab initio models were calculated using GASBOR[51]. The superposition of a predicted *Sa*NsrF model (see below) was done using the program SUPCOMB[56].

Structural models of SaNsrF complexes. As an experimental *Sa*NsrF structure is not available, a homology model was constructed using the template-based protein structure prediction program TopModel[52] and the *Sa*$NsrF_{WT}$ sequence as input (NCBI Reference Sequence: WP_000923535.1). In order to build a *Sa*NsrF model arranged in a dimeric assembly with substrate (ATP) and cofactor (Mg^{2+}) bound, starting from the *Sa*$NsrF_{WT}$ monomer in the *apo* state, a search for sequence similarity and structural properties was performed on the Protein Data Bank. The results were filtered according to the following criteria: sequence identity ≥ 33% and E-value cutoff 0.001 as determined by BLAST[77]; oligomeric state equals 2; sequence length of 250 ± 50 residues; resolution ≤ 2 Å. Out of six results, only one (PDB ID: 1L2T[28]) is crystallized as a functionally active "ATP sandwich" symmetrical dimer and was therefore used as a reference. Since ATP is bound at the interface of the dimer and its binding is influenced by both protein subunits, both protein–ligand and protein–protein docking would be particularly challenging in this case. Hence, we constructed first the *Sa*$NsrF_{WT}$ dimer in the *apo* form and the ATP/Mg^{2+}-bound form subsequently.

To do so, protein–protein docking was performed with the program HADDOCK[78,79], using distances between respective three residues that bridge the two subunits together with H-bond interactions as restraints (S40/S43, R153/R152 and D177/D176, for PDB ID 1L2T/*Sa*$NsrF_{WT}$ sequences, respectively). The most similar docking solution to the reference PDB ID 1L2T was used for further modeling steps.

Both, *Sa*$NsrF_{WT}$ monomer and dimer structures were preprocessed with the Protein Preparation Wizard[80] of Schrödinger's Maestro Suite. Since the residues at the binding sites are highly conserved, ATP and Mg^{2+} are considered to bind in a very similar way as in PDB ID 1L2T. Thus, their coordinates were copied from the reference into the *Sa*$NsrF_{WT}$ model after alignment to one protein subunit. Residues located ≤ 5 Å away from the ATP molecules were energy-minimized using the OPLS 2005 force field[81] with standard cutoff values for van der Waals, electrostatic, and H-bond interactions, until the average RMSD of non-hydrogen atoms reaches 0.30 Å. Bond orders as well as missing hydrogen atoms were assigned, and the H-bond network was optimized. Finally, residue 202 was substituted to construct the *Sa*$NsrF_{H202A}$ variant of the monomer and dimer.

Molecular dynamics simulations. In order to validate the modeled protein–protein interface and the ATP binding mode, and to investigate the impact of the *Sa*$NsrF_{H202A}$ substitution on structural dynamics, a set of MD simulations was performed using Amber 2019[82]. Four different ATP/Mg^{2+}-bound *Sa*NsrF systems were prepared for this with the LEaP program[83]: monomer and dimer, both for *Sa*$NsrF_{WT}$ and *Sa*$NsrF_{H202A}$.

After establishing charge neutrality by adding sodium counter ions, each system was placed in a truncated octahedral box of TIP3P[84] water with a distance of the nearest atom to the border of the box of ≥ 11 Å. Structural relaxation, thermalization, and production runs of MD simulations were conducted with pmemd.cuda[85] using the ff14SB force field[86] for the protein, Joung-Cheatham parameters[87] for ions, and available ATP parameters[88]. For each starting complex, five independent replicas of 500 ns length each were performed, resulting in a cumulative simulation time of 10 µs. In order to set up independent replicas and obtain slightly different starting structures, the target temperature was set to different values during thermalization (299.8 K, 299.9 K, 300.0 K, 300.1 K, 300.2 K and 300.3 K). A detailed description of the thermalization protocol can be found elsewhere[89]. The analysis of the MD trajectories was carried out with cpptraj[90] on snapshots extracted every 1 ns. All the MD-generated conformations were clustered applying a hierarchical agglomerative approach and an RMSD cutoff value of 4 Å. The representative structure of the *Sa*$NsrF_{WT}$ monomer was compared to the experimentally determined SAXS density.

The representative structure of the most populated cluster for the *Sa*$NsrF_{WT}$ dimer was used to calculate the electrostatic potential with the Adaptive Poisson-Boltzmann Solver (APBS) software package[49] as implemented in PyMOL[91]. Dielectric constants (ε) of 2.0 and 78.0 were used, respectively, for the protein and for water, and the concentration of monovalent cations and anions was set to 0.15 M.

To measure structural mobility, we computed the residue-wise root-mean-square fluctuation (RMSF) of backbone atoms. Structural changes over time, both for the *apo* *Sa*NsrF proteins and the ATP/Mg^{2+}-bound form, were detected calculating the root-mean-square deviation of atomic positions (RMSD) compared to the initial structure. To describe the changes occurring at the level of the interface, we performed two analyses: (I) measurement of the distance between the center of mass of two residues located in opposite subunits at the center of the interface (S43 and S146); (II) H-bond analysis (i) in terms of the total number of interactions between

two subunits ($SaNsrF_A$–$SaNsrF_B$) and between protein and ligands ($SaNsrF$-(ATP-Mg^{2+})) and ii) residue-wise H-bound occupancy between residues of the two subunits ($SaNsrF_A$–$SaNsrF_B$), allowing to identify which residues perform more frequent H-bonds throughout the simulations. For this analysis, only H-bonds with the following criteria were considered: occupancy between specific donor and acceptor > 1%; H-bond present in at least two replicas of the same system; H-bonds between two residues with residue-wise occupancy > 10% in at least one system.

Molecular docking of other NTPs. To predict the binding mode of other NTPs in complex with the $SaNsrF_{WT}$ dimer, molecular docking was performed. The starting points for these calculations were the five structures resulting from thermalization and equilibration steps, then used also for independent MD simulations replicas (production).

First, for each binding site a cubic grid of 20 Å length centered on the respective ATP molecule was built in the Maestro platform[92], for a total of 10 different grids. Then, starting from the ATP structures, other NTPs were built (GTP, CTP and UTP) by modifying the nucleobase. The generated conformations were refined and scored with the Glide-Extra precision (XP) mode of Glide[93]. Only the best solution for each NTP in each grid was considered. The Coulomb interaction energy (ecoul) and the van der Waals energy (evdw), components of the XP GlideScore scoring function, were computed, and used to describe the enthalpic contribution of binding.

Data availability

We upload the SAXS data and the corresponding model of *Sa*NsrF to the Small Angle Scattering Biological Data Bank (SASBDB)[54,55], with the accession code SASDJR3.

Received: 19 July 2020; Accepted: 27 August 2020
Published online: 16 September 2020

References

1. Gould, K. Antibiotics: from prehistory to the present day. *J. Antimicrob. Chemother.* **71**, 572–575. https://doi.org/10.1093/jac/dkv484 (2016).
2. Meade, E., Slattery, M. A. & Garvey, M. Bacteriocins, potent antimicrobial peptides and the fight against multi drug resistant species: resistance is futile?. *Antibiotics* https://doi.org/10.3390/antibiotics9010032 (2020).
3. Cotter, P. D., Hill, C. & Ross, R. P. Bacterial lantibiotics: strategies to improve therapeutic potential. *Curr. Protein Pept. Sci.* **6**, 61–75. https://doi.org/10.2174/1389203053027584 (2005).
4. Clemens, R., Zaschke-Kriesche, J., Khosa, S. & Smits, S. H. J. Insight into two ABC transporter Families involved in lantibiotic resistance. *Front. Mol. Biosci.* **4**, 91. https://doi.org/10.3389/fmolb.2017.00091 (2017).
5. Bierbaum, G. & Sahl, H. G. Lantibiotics: mode of action, biosynthesis and bioengineering. *Curr. Pharm. Biotechnol.* **10**, 2–18. https://doi.org/10.2174/138920109787048616 (2009).
6. Chatterjee, C., Paul, M., Xie, L. & van der Donk, W. A. Biosynthesis and mode of action of lantibiotics. *Chem. Rev.* **105**, 633–684. https://doi.org/10.1021/cr030105v (2005).
7. Jabes, D. *et al.* Efficacy of the new lantibiotic NAI-107 in experimental infections induced by multidrug-resistant Gram-positive pathogens. *Antimicrob. Agents Chemother.* **55**, 1671–1676. https://doi.org/10.1128/AAC.01288-10 (2011).
8. Reiners, J. *et al.* The N-terminal region of nisin is important for the BceAB-type ABC transporter NsrFP from *Streptococcus agalactiae* COH1. *Front. Microbiol.* **8**, 1643. https://doi.org/10.3389/fmicb.2017.01643 (2017).
9. Malin, J. J. & de Leeuw, E. Therapeutic compounds targeting Lipid II for antibacterial purposes. *Infect. Drug Resist.* **12**, 2613–2625. https://doi.org/10.2147/IDR.S215070 (2019).
10. Breukink, E. *et al.* Use of the cell wall precursor lipid II by a pore-forming peptide antibiotic. *Science* **286**, 2361–2364. https://doi.org/10.1126/science.286.5448.2361 (1999).
11. Hasper, H. E., de Kruijff, B. & Breukink, E. Assembly and stability of nisin-lipid II pores. *Biochemistry* **43**, 11567–11575. https://doi.org/10.1021/bi049476b (2004).
12. AlKhatib, Z. *et al.* The C-terminus of nisin is important for the ABC transporter NisFEG to confer immunity in *Lactococcus lactis*. *Microbiologyopen* **3**, 752–763. https://doi.org/10.1002/mbo3.205 (2014).
13. Draper, L. A., Cotter, P. D., Hill, C. & Ross, R. P. Lantibiotic resistance. *Microbiol. Mol. Biol. Rev.* **79**, 171–191. https://doi.org/10.1128/MMBR.00051-14 (2015).
14. Ohki, R. *et al.* The BceRS two-component regulatory system induces expression of the bacitracin transporter, BceAB, Bacillus subtilis. *Mol. Microbiol.* **49**, 1135–1144. https://doi.org/10.1046/j.1365-2958.2003.03653.x (2003).
15. Podlesek, Z. *et al. Bacillus licheniformis* bacitracin-resistance ABC transporter: relationship to mammalian multidrug resistance. *Mol. Microbiol.* **16**, 969–976. https://doi.org/10.1111/j.1365-2958.1995.tb02322.x (1995).
16. Khosa, S., AlKhatib, Z. & Smits, S. H. NSR from *Streptococcus agalactiae* confers resistance against nisin and is encoded by a conserved nsr operon. *Biol. Chem.* **394**, 1543–1549. https://doi.org/10.1515/hsz-2013-0167 (2013).
17. Khosa, S. *et al.* Structural basis of lantibiotic recognition by the nisin resistance protein from *Streptococcus agalactiae*. *Sci. Rep.* **6**, 18679. https://doi.org/10.1038/srep18679 (2016).
18. Khosa, S., Hoeppner, A., Gohlke, H., Schmitt, L. & Smits, S. H. Structure of the response regulator NsrR from *Streptococcus agalactiae*, which is involved in lantibiotic resistance. *PLoS ONE* **11**, e0149903. https://doi.org/10.1371/journal.pone.0149903 (2016).
19. Kerr, I. D. Structure and association of ATP-binding cassette transporter nucleotide-binding domains. *Biochim. Biophys. Acta* **1561**, 47–64. https://doi.org/10.1016/s0304-4157(01)00008-9 (2002).
20. Lawson, J., O'Mara, M. L. & Kerr, I. D. Structure-based interpretation of the mutagenesis database for the nucleotide binding domains of P-glycoprotein. *Biochim. Biophys. Acta* **1778**, 376–391. https://doi.org/10.1016/j.bbamem.2007.10.021 (2008).
21. Walker, J. E., Saraste, M., Runswick, M. J. & Gay, N. J. Distantly related sequences in the alpha- and beta-subunits of ATP synthase, myosin, kinases and other ATP-requiring enzymes and a common nucleotide binding fold. *EMBO J.* **1**, 945–951 (1982).
22. Szollosi, D., Rose-Sperling, D., Hellmich, U. A. & Stockner, T. Comparison of mechanistic transport cycle models of ABC exporters. *Biochim. Biophys. Acta Biomembr.* **818–832**, 2018. https://doi.org/10.1016/j.bbamem.2017.10.028 (1860).
23. Schmitt, L., Benabdelhak, H., Blight, M. A., Holland, I. B. & Stubbs, M. T. Crystal structure of the nucleotide-binding domain of the ABC-transporter haemolysin B: identification of a variable region within ABC helical domains. *J. Mol. Biol.* **330**, 333–342. https://doi.org/10.1016/s0022-2836(03)00592-8 (2003).
24. Schmitt, L. & Tampe, R. Structure and mechanism of ABC transporters. *Curr. Opin. Struct. Biol.* **12**, 754–760. https://doi.org/10.1016/s0959-440x(02)00399-8 (2002).
25. Wilkens, S. Structure and mechanism of ABC transporters. *F1000Prime Rep* **7**, 14. https://doi.org/10.12703/P7-14 (2015).

26. Hanekop, N., Zaitseva, J., Jenewein, S., Holland, I. B. & Schmitt, L. Molecular insights into the mechanism of ATP-hydrolysis by the NBD of the ABC-transporter HlyB. *FEBS Lett.* **580**, 1036–1041. https://doi.org/10.1016/j.febslet.2005.11.012 (2006).
27. Schmees, G., Stein, A., Hunke, S., Landmesser, H. & Schneider, E. Functional consequences of mutations in the conserved "signature sequence" of the ATP-binding-cassette protein MalK. *Eur J. Biochem.* **266**, 420–430. https://doi.org/10.1046/j.1432-1327.1999.00871.x (1999).
28. Smith, P. C. *et al.* ATP binding to the motor domain from an ABC transporter drives formation of a nucleotide sandwich dimer. *Mol. Cell.* **10**, 139–149 (2002).
29. Chen, J., Lu, G., Lin, J., Davidson, A. L. & Quiocho, F. A. A tweezers-like motion of the ATP-binding cassette dimer in an ABC transport cycle. *Mol. Cell.* **12**, 651–661. https://doi.org/10.1016/j.molcel.2003.08.004 (2003).
30. Locher, K. P. Structure and mechanism of ABC transporters. *Curr. Opin. Struct. Biol.* **14**, 426–431. https://doi.org/10.1016/j.sbi.2004.06.005 (2004).
31. Szollosi, D., Szakacs, G., Chiba, P. & Stockner, T. Dissecting the forces that dominate dimerization of the nucleotide binding domains of ABCB1. *Biophys. J.* **114**, 331–342. https://doi.org/10.1016/j.bpj.2017.11.022 (2018).
32. Wagner, M., Smits, S. H. J. & Schmitt, L. In vitro NTPase activity of highly purified Pdr5, a major yeast ABC multidrug transporter. *Sci. Rep.* **9**, 7761. https://doi.org/10.1038/s41598-019-44327-8 (2019).
33. Sahin, E. & Roberts, C. J. Size-exclusion chromatography with multi-angle light scattering for elucidating protein aggregation mechanisms. *Methods Mol. Biol.* **899**, 403–423. https://doi.org/10.1007/978-1-61779-921-1_25 (2012).
34. Greller, G., Horlacher, R., DiRuggiero, J. & Boos, W. Molecular and biochemical analysis of MalK, the ATP-hydrolyzing subunit of the trehalose/maltose transport system of the hyperthermophilic archaeon *Thermococcus litoralis*. *J. Biol. Chem.* **274**, 20259–20264. https://doi.org/10.1074/jbc.274.29.20259 (1999).
35. Nikaido, K., Liu, P. Q. & Ames, G. F. Purification and characterization of HisP, the ATP-binding subunit of a traffic ATPase (ABC transporter), the histidine permease of *Salmonella typhimurium*. Solubility, dimerization, and ATPase activity. *J. Biol. Chem.* **272**, 27745–27752. https://doi.org/10.1074/jbc.272.44.27745 (1997).
36. Zaitseva, J. *et al.* Functional characterization and ATP-induced dimerization of the isolated ABC-domain of the haemolysin B transporter. *Biochemistry* **44**, 9680–9690. https://doi.org/10.1021/bi0506122 (2005).
37. Kolaczkowski, M., Sroda-Pomianek, K., Kolaczkowska, A. & Michalak, K. A conserved interdomain communication pathway of pseudosymmetrically distributed residues affects substrate specificity of the fungal multidrug transporter Cdr1p. *Biochim Biophys Acta* **479–490**, 2013. https://doi.org/10.1016/j.bbamem.2012.10.024 (1828).
38. Zaitseva, J., Jenewein, S., Jumpertz, T., Holland, I. B. & Schmitt, L. H662 is the linchpin of ATP hydrolysis in the nucleotide-binding domain of the ABC transporter HlyB. *EMBO J.* **24**, 1901–1910. https://doi.org/10.1038/sj.emboj.7600657 (2005).
39. Zhou, Y., Ojeda-May, P. & Pu, J. H-loop histidine catalyzes ATP hydrolysis in the *E. coli* ABC-transporter HlyB. *Phys Chem Chem Phys* **15**, 15811–15815. https://doi.org/10.1039/c3cp50965f (2013).
40. Lagedroste, M., Reiners, J., Smits, S. H. J. & Schmitt, L. Systematic characterization of position one variants within the lantibiotic nisin. *Sci. Rep.* **9**, 935. https://doi.org/10.1038/s41598-018-37532-4 (2019).
41. Davidson, A. L., Laghaeian, S. S. & Mannering, D. E. The maltose transport system of *Escherichia coli* displays positive cooperativity in ATP hydrolysis. *J. Biol. Chem.* **271**, 4858–4863 (1996).
42. Senior, A. E. & Bhagat, S. P-glycoprotein shows strong catalytic cooperativity between the two nucleotide sites. *Biochemistry* **37**, 831–836. https://doi.org/10.1021/bi9719962 (1998).
43. Zaitseva, J. *et al.* A structural analysis of asymmetry required for catalytic activity of an ABC-ATPase domain dimer. *EMBO J.* **25**, 3432–3443. https://doi.org/10.1038/sj.emboj.7601208 (2006).
44. Okada, U. *et al.* Crystal structure of tripartite-type ABC transporter MacB from *Acinetobacter baumannii*. *Nat. Commun.* **8**, 1336. https://doi.org/10.1038/s41467-017-01399-2 (2017).
45. Yang, H. B. *et al.* Structure of a MacAB-like efflux pump from *Streptococcus pneumoniae*. *Nat. Commun.* **9**, 196. https://doi.org/10.1038/s41467-017-02741-4 (2018).
46. Mulnaes, D. & Gohlke, H. TopScore: using deep neural networks and large diverse data sets for accurate protein model quality assessment. *J. Chem. Theory. Comput.* **14**, 6117–6126. https://doi.org/10.1021/acs.jctc.8b00690 (2018).
47. Mariani, V., Biasini, M., Barbato, A. & Schwede, T. lDDT: a local superposition-free score for comparing protein structures and models using distance difference tests. *Bioinformatics* **29**, 2722–2728. https://doi.org/10.1093/bioinformatics/btt473 (2013).
48. Ishii, S., Yano, T., Okamoto, A., Murakawa, T. & Hayashi, H. Boundary of the nucleotide-binding domain of *Streptococcus* ComA based on functional and structural analysis. *Biochemistry* **52**, 2545–2555. https://doi.org/10.1021/bi3017069 (2013).
49. Baker, N. A., Sept, D., Joseph, S., Holst, M. J. & McCammon, J. A. Electrostatics of nanosystems: application to microtubules and the ribosome. *Proc. Natl. Acad. Sci. USA* **98**, 10037–10041. https://doi.org/10.1073/pnas.181342398 (2001).
50. Damas, J. M., Oliveira, A. S., Baptista, A. M. & Soares, C. M. Structural consequences of ATP hydrolysis on the ABC transporter NBD dimer: molecular dynamics studies of HlyB. *Protein Sci.* **20**, 1220–1230. https://doi.org/10.1002/pro.650 (2011).
51. Svergun, D. I., Petoukhov, M. V. & Koch, M. H. Determination of domain structure of proteins from X-ray solution scattering. *Biophys J* **80**, 2946–2953. https://doi.org/10.1016/S0006-3495(01)76260-1 (2001).
52. Mulnaes, D. *et al.* TopModel: template-based protein structure prediction at low sequence identity using top-down consensus and deep neural networks. *J. Chem. Theory Comput.* **16**, 1953–1967. https://doi.org/10.1021/acs.jctc.9b00825 (2020).
53. Svergun, D., Barberato, C. & Koch, M. H. J. CRYSOL: a program to evaluate x-ray solution scattering of biological macromolecules from atomic coordinates. *J. Appl. Crystallogr.* **28**, 768–773. https://doi.org/10.1107/S0021889895007047 (1995).
54. Valentini, E., Kikhney, A. G., Previtali, G., Jeffries, C. M. & Svergun, D. I. SASBDB, a repository for biological small-angle scattering data. *Nucleic Acids Res.* **43**, D357-363. https://doi.org/10.1093/nar/gku1047 (2015).
55. Kikhney, A. G., Borges, C. R., Molodenskiy, D. S., Jeffries, C. M. & Svergun, D. I. SASBDB: towards an automatically curated and validated repository for biological scattering data. *Protein Sci.* **29**, 66–75. https://doi.org/10.1002/pro.3731 (2020).
56. Kozin, M. B. & Svergun, D. I. Automated matching of high- and low-resolution structural models. *J. Appl. Crystallogr.* **34**, 33–41. https://doi.org/10.1107/S0021889800014126 (2001).
57. Collins, B., Curtis, N., Cotter, P. D., Hill, C. & Ross, R. P. The ABC transporter AnrAB contributes to the innate resistance of *Listeria monocytogenes* to nisin, bacitracin, and various beta-lactam antibiotics. *Antimicrob. Agents Chemother.* **54**, 4416–4423. https://doi.org/10.1128/AAC.00503-10 (2010).
58. Hiron, A., Falord, M., Valle, J., Debarbouille, M. & Msadek, T. Bacitracin and nisin resistance in *Staphylococcus aureus*: a novel pathway involving the BraS/BraR two-component system (SA2417/SA2418) and both the BraD/BraE and VraD/VraE ABC transporters. *Mol. Microbiol.* **81**, 602–622. https://doi.org/10.1111/j.1365-2958.2011.07735.x (2011).
59. Popella, P. *et al.* VraH is the third component of the *Staphylococcus aureus* VraDEH system involved in gallidermin and daptomycin resistance and pathogenicity. *Antimicrob. Agents Chemother.* **60**, 2391–2401. https://doi.org/10.1128/AAC.02865-15 (2016).
60. Staron, A., Finkeisen, D. E. & Mascher, T. Peptide antibiotic sensing and detoxification modules of *Bacillus subtilis*. *Antimicrob. Agents Chemother.* **55**, 515–525. https://doi.org/10.1128/AAC.00352-10 (2011).
61. Yang, J., Yu, M., Jan, Y. N. & Jan, L. Y. Stabilization of ion selectivity filter by pore loop ion pairs in an inwardly rectifying potassium channel. *Proc. Natl. Acad. Sci. USA* **94**, 1568–1572. https://doi.org/10.1073/pnas.94.4.1568 (1997).
62. Ramaen, O. *et al.* Structure of the human multidrug resistance protein 1 nucleotide binding domain 1 bound to Mg2+/ATP reveals a non-productive catalytic site. *J. Mol. Biol.* **359**, 940–949. https://doi.org/10.1016/j.jmb.2006.04.005 (2006).

63. Benabdelhak, H. *et al.* Positive co-operative activity and dimerization of the isolated ABC ATPase domain of HlyB from *Escherichia coli*. *Biochem. J.* **386**, 489–495. https://doi.org/10.1042/BJ20041282 (2005).
64. Ramaen, O., Sizun, C., Pamlard, O., Jacquet, E. & Lallemand, J. Y. Attempts to characterize the NBD heterodimer of MRP1: transient complex formation involves Gly771 of the ABC signature sequence but does not enhance the intrinsic ATPase activity. *Biochem. J.* **391**, 481–490. https://doi.org/10.1042/BJ20050897 (2005).
65. Schultz, K. M., Merten, J. A. & Klug, C. S. Characterization of the E506Q and H537A dysfunctional mutants in the *E. coli* ABC transporter MsbA. *Biochemistry* **50**, 3599–3608. https://doi.org/10.1021/bi101666p (2011).
66. Osorio, H. *et al.* H2O2, but not menadione, provokes a decrease in the ATP and an increase in the inosine levels in *Saccharomyces cerevisiae*: an experimental and theoretical approach. *Eur. J. Biochem.* **270**, 1578–1589. https://doi.org/10.1046/j.1432-1033.2003.03529.x (2003).
67. Buckstein, M. H., He, J. & Rubin, H. Characterization of nucleotide pools as a function of physiological state in *Escherichia coli*. *J. Bacteriol.* **190**, 718–726. https://doi.org/10.1128/JB.01020-07 (2008).
68. Bochner, B. R. & Ames, B. N. Complete analysis of cellular nucleotides by two-dimensional thin layer chromatography. *J. Biol. Chem.* **257**, 9759–9769 (1982).
69. Reimann, S. *et al.* Interdomain regulation of the ATPase activity of the ABC transporter haemolysin B from *Escherichia coli*. *Biochem. J.* **473**, 2471–2483. https://doi.org/10.1042/BCJ20160154 (2016).
70. Lagedroste, M., Reiners, J., Smits, S. H. J. & Schmitt, L. Impact of the nisin modification machinery on the transport kinetics of NisT. *Sci. Rep.* **10**, 12295. https://doi.org/10.1038/s41598-020-69225-2 (2020).
71. Zheng, S., Nagao, J. I., Nishie, M., Zendo, T. & Sonomoto, K. ATPase activity regulation by leader peptide processing of ABC transporter maturation and secretion protein, NukT, for lantibiotic nukacin ISK-1. *Appl. Microbiol. Biotechnol.* **102**, 763–772. https://doi.org/10.1007/s00253-017-8645-2 (2018).
72. Hanahan, D. Studies on transformation of *Escherichia coli* with plasmids. *J. Mol. Biol.* **166**, 557–580. https://doi.org/10.1016/s0022-2836(83)80284-8 (1983).
73. Franke, D. *et al.* ATSAS 2.8: a comprehensive data analysis suite for small-angle scattering from macromolecular solutions. *J. Appl. Crystallogr.* **50**, 1212–1225. https://doi.org/10.1107/S1600576717007786 (2017).
74. Konarev, P. V., Volkov, V. V., Sokolova, A. V., Koch, M. H. J. & Svergun, D. I. PRIMUS: a Windows PC-based system for small-angle scattering data analysis. *J. Appl. Crystallogr.* **36**, 1277–1282. https://doi.org/10.1107/S0021889803012779 (2003).
75. Guinier, A. Diffraction of x-rays of very small angles-application to the study of ultramicroscopic phenomenon. *Ann. Phys.* **12**, 161–237 (1939).
76. Svergun, D. I. Determination of the regularization parameter in indirect-transform methods using perceptual criteria. *J. Appl. Crystallogr.* **25**, 495–503. https://doi.org/10.1107/S0021889892001663 (1992).
77. Altschul, S. F., Gish, W., Miller, W., Myers, E. W. & Lipman, D. J. Basic local alignment search tool. *J. Mol. Biol.* **215**, 403–410. https://doi.org/10.1016/S0022-2836(05)80360-2 (1990).
78. Dominguez, C., Boelens, R. & Bonvin, A. M. HADDOCK: a protein-protein docking approach based on biochemical or biophysical information. *J. Am. Chem. Soc.* **125**, 1731–1737. https://doi.org/10.1021/ja026939x (2003).
79. van Zundert, G. C. P. *et al.* The HADDOCK2.2 web server: user-friendly integrative modeling of biomolecular complexes. *J. Mol. Biol.* **428**, 720–725. https://doi.org/10.1016/j.jmb.2015.09.014 (2016).
80. Schrödinger Release 2017-1: Schrödinger Suite 2017-1 Protein Preparation Wizard, Schrödinger, LLC, New York, NY, 2017.
81. Banks, J. L. *et al.* Integrated modeling program, applied chemical theory (IMPACT). *J. Comput. Chem.* **26**, 1752–1780. https://doi.org/10.1002/jcc.20292 (2005).
82. Case, D. A. *et al. Amber* (University of California, San Francisco, 2019).
83. Schafmeister Ceaf, R. W. & Romanovski, V. *LEaP* (University of California, San Francisco, 1995).
84. Jorgensen, W. L., Chandrasekhar, J., Madura, J. D., Impey, R. W. & Klein, M. L. Comparison of simple potential functions for simulating liquid water. *J. Chem. Phys.* **79**, 926–935. https://doi.org/10.1063/1.445869 (1983).
85. Salomon-Ferrer, R., Gotz, A. W., Poole, D., Le Grand, S. & Walker, R. C. Routine microsecond molecular dynamics simulations with AMBER on GPUs 2 explicit solvent particle mesh ewald. *J. Chem. Theory Comput.* **9**, 3878–3888. https://doi.org/10.1021/ct400314y (2013).
86. Maier, J. A. *et al.* ff14SB: improving the accuracy of protein side chain and backbone parameters from ff99SB. *J. Chem. Theory. Comput.* **11**, 3696–3713. https://doi.org/10.1021/acs.jctc.5b00255 (2015).
87. Joung, I. S. & Cheatham, T. E. 3rd. Determination of alkali and halide monovalent ion parameters for use in explicitly solvated biomolecular simulations. *J. Phys. Chem. B* **112**, 9020–9041. https://doi.org/10.1021/jp8001614 (2008).
88. Meagher, K. L., Redman, L. T. & Carlson, H. A. Development of polyphosphate parameters for use with the AMBER force field. *J. Comput. Chem.* **24**, 1016–1025. https://doi.org/10.1002/jcc.10262 (2003).
89. Frieg, B. *et al.* Molecular mechanisms of glutamine synthetase mutations that lead to clinically relevant pathologies. *PLoS Comput. Biol.* **12**, e1004693. https://doi.org/10.1371/journal.pcbi.1004693 (2016).
90. Roe, D. R. & Cheatham, T. E. 3rd. PTRAJ and CPPTRAJ: SOFTWARE for processing and analysis of molecular dynamics trajectory data. *J. Chem. Theory Comput.* **9**, 3084–3095. https://doi.org/10.1021/ct400341p (2013).
91. The PyMOL Molecular Graphics System, Version 2.0 Schrödinger, LLC.
92. Schrödinger Release 2020-2: Maestro, Schrödinger, LLC, New York (2020).
93. Schrödinger Release 2020-2: Schrödinger Suite 2020-2 Glide, Schrödinger, LLC, New York (2020).

Acknowledgements

We thank Lutz Schmitt for his continuous support and the members of the Institute of Biochemistry for valuable discussions. This work has been funded by the Deutsche Forschungsgemeinschaft (DFG, German Research Foundation)—Project number 270650915 (Research Training Group GRK2158, TP4a to H.G. and TP4b to S.S.). The Center for Structural studies is funded by the DFG (Grant Number 417919780 and INST 208/761-1 FUGG to S.S.). H.G. is grateful for computational support by the "Zentrum für Informations und Medientechnologie" at the Heinrich-Heine-Universität Düsseldorf and the computing time provided by the John von Neumann Institute for Computing (NIC) to H.G. on the supercomputer JUWELS at Jülich Supercomputing Centre (JSC) (user IDs: HKF7).

Author contributions

S.H.J.S. conceived and coordinated the study and evaluated all data; F.F performed overexpression, purification and functional characterization of the *Sa*NsrF enzymes and contributed to the writing; J.R. performed the SAXS and data analysis, and contributed to the writing; D.T.H., J.S. and J.G. did the cloning and established the purification protocol; H.G. conceptualized and supervised molecular modeling and simulation, analyzed the

data, and contributed to the writing; N.P. performed molecular modeling and simulation, analyzed the data, and contributed to the writing.

Funding

This work has been funded by the Deutsche Forschungsgemeinschaft (DFG, German Research Foundation)—Project Number 270650915 (Research Training Group GRK2158, TP4a to H.G. and TP4b to S.S.). The Center for Structural studies is funded by the DFG (Grant Number 417919780 and INST 208/761-1 FUGG to S.S.). H.G. is grateful for computational support by the "Zentrum für Informations und Medientechnologie" at the Heinrich-Heine-Universität Düsseldorf and the computing time provided by the John von Neumann Institute for Computing (NIC) to H.G. on the supercomputer JUWELS at Jülich Supercomputing Centre (JSC) (user IDs: HKF7). Open Access funding provided by Projekt DEAL.

Competing interests

The authors declare no competing interests.

Additional information

Supplementary information is available for this paper at https://doi.org/10.1038/s41598-020-72237-7.

Correspondence and requests for materials should be addressed to S.H.J.S.

Reprints and permissions information is available at www.nature.com/reprints.

Publisher's note Springer Nature remains neutral with regard to jurisdictional claims in published maps and institutional affiliations.